

Work hardening analysis in a lean duplex stainless Steel 2304 after low deformation by cold rolling

Davi Silva Alves ¹ 
Daniella Gomes Rodrigues ¹
Dagoberto Brandão Santos ^{1*}

Abstract

The deformation mechanism of lean duplex stainless steel (LDSS) is overly complex not only by their dual phase microstructure, but also due to metastable austenite, which can deform by different mechanisms and transform to martensite by strain. The purpose of this study was to investigate the mechanisms of deformation by tensile test on low deformed cold-rolled samples (4%-22%) of a 2304 LDSS. The microstructure was analyzed by X-ray diffraction, optical microscopy, electron backscattered diffraction and transmission electron microscopy. It was observed the formation of mechanical twinning, ϵ -martensite, and α' -martensite which evidenced the TRIP effect. The strain hardening rate was calculated and analyzed by Holomon and Crussard-Jaoul modeling together with instantaneous strain hardening exponent, and three operating mechanisms were observed: twinning, dislocations slipping, and strain induced martensite formation (SIM). Brass texture had compromised SIM transformation. The fractography analysis of tensile specimens showed quasi-cleavage occurrence, and dimples formation for this range of pre-deformation.

Keywords: Lean-duplex stainless steel; TRIP effect; Twinning; Strain-hardening; Stacking fault energy.

1 Introduction

Duplex stainless steels (DSS), which possess an excellent combination of corrosion resistance and mechanical properties, are widely applied to many industrial fields such as pollution control, oil and gas, petrochemical, and ocean engineering [1]. DSS have established themselves as a great alternative in aggressive environments in the chemical, petrochemical, and cellulose industrial sectors, as they have a good performance. They present a dual-phase microstructure, usually in the proportion of 50% of austenite and ferrite [2,3].

To obtain a lower cost, and thus a greater competitiveness in the market, as well as environmental issues, the concept of lean duplex stainless steel was developed, which has smaller amount of the elements nickel and molybdenum, being replaced by manganese and nitrogen [2]. The addition of these elements makes the austenite metastable, changing its stacking fault energy (SFE) value [4].

By presenting this dual-phase microstructure, the plastic deformation mechanisms of this steel become more complex than those of single-phase materials, such ferritic or austenitic stainless steels [1]. SFE will strongly influence the austenite deformation mechanisms. This can occur by slipping in crystalline planes due to dislocations movement, formation of deformation twins and strain-induced martensite (SIM). The latter mechanism being associated with the TRIP effect. The formation of martensite in this type of DSS can

occur in two ways: (i) through the direct transformation of austenite to martensite $\gamma \rightarrow \alpha'$, or (ii) through the intermediate phase, the hexagonal ϵ -martensite, that is, $\gamma \rightarrow \epsilon \rightarrow \alpha'$. Some studies have observed these two transformation mechanisms in 2304 lean duplex stainless steel [5,6]. However, there is still a plenty of space to explore the phenomenon and how it acts on the work hardening behavior and which mechanisms are operating along the plastic deformation of this alloy, mainly during low deformation intensity, in present case by cold rolling processing. One important point to consider is the influence of ϵ -martensite on the strain hardening behavior of the alloy.

2 Materials and methods

The material used in this study was a hot-rolled 2304 LDSS steel with the chemical composition according to Table 1. The material as-received (AR) was industrially hot-rolled to a thickness of 4.0 mm and then homogenized at 1050°C for 180 s and water quenching.

The samples (150x100x4 mm) were cold rolled with 4%, 12%, 17% and 22% of thickness reduction in successive passes on a laboratory rolling mill at room temperature ($\sim 25^\circ\text{C}$), and a speed of 6.25 m.min⁻¹. These samples were called 4%-CR, 12%-CR, 17%-CR and 22%-CR.

¹Departamento de Engenharia Metalúrgica e de Materiais, Universidade Federal de Minas Gerais – UFMG, Belo Horizonte, MG, Brasil.

*Corresponding author: dsantos@demet.ufmg.br



2176-1523 © 2022. Alves et al. Published by ABM. This is an Open Access article distributed under the terms of the Creative Commons Attribution License, which permits unrestricted use, distribution, and reproduction in any medium, provided the original work is properly cited.

The mechanical properties of the cold-rolled samples were evaluated by averaging the uniaxial tensile test (3 specimens) at a constant strain rate of 10^{-3} s $^{-1}$, using a universal mechanical test machine, Instron 5582, and the Blue Hill software. The tests were performed at room temperature in accordance to ASTM E8 (2015) and the samples were machined in accordance with ASTM A370, sub-size dimensions [7]. Figure 1 show a scheme in tensile test specimen for withdraw of the metallographic samples along the rolling plane. These samples were called AR-T, 4%CR-T, 12%CR-T, 17%CR-T, 22%CR-T.

For microstructural analysis of the cold rolled state, the samples were characterized along the longitudinal section, and for tensile after cold rolling, the samples were characterized along normal section, i.e. rolling plane, both using a backscattered electron diffraction detector (EBSD) coupled to a scanning electron microscope (SEM) Quanta FEG 3D. Samples analyzed via EBSD were prepared by mechanical grinding and polishing, followed by final polishing with colloidal silica with 0.04 μ m particles for 90 min.

Data acquisition by backscattered electron diffraction was performed with an accelerating voltage of 30 kV, working distance of 20 mm, and a pass of 53 nm. The data obtained were processed and analyzed using the TSL-EDAX OIMTM software. The chemical composition of the γ phase was measured using an energy dispersive X-ray spectrometer, EDS.

The X-ray diffraction was obtained at room temperature, using Cu(K α) radiation, passing of 0.005 $^\circ$ for 1 s, and 2 θ angular interval of 10 $^\circ$ -100 $^\circ$ in a Panalytical Empyrean diffractometer. The phase volume fraction estimation was performed through the integration method of the α peaks defined by the planes (110), (200), (211) and (220), and γ , defined by the planes (111), (200), (220) and (311). The deformed samples were also studied by transmission electron microscopy (TEM) using a Tecnai G2-20 – Super Twin FEI microscope, operating at 200 kV. The samples

were grounded and polished to approximately 80 μ m of thickness. Subsequently, discs of 3.0 mm in diameter were cut using a disc puncher instrument. The discs were polished in diamond paste to a thickness of approximately 50 μ m. These discs were then electrolytically drilled in a Tenupol 5 Struers, using a solution of HClO $_4$:C $_2$ H $_4$ O $_2$ = 1:19 with a voltage of 20 V at -10 $^\circ$ C.

3 Results and discussion

3.1 Microstructural analysis

The microstructure of the samples after tensile test is shown in Figure 2. The microstructures are composed by a continuous matrix of ferrite (α), darker on the micrograph, alternating with lenticular-shaped austenite (γ), typical of rolled DSS [6,8-10]. Brighter phase with needles morphology inside γ grains, like martensite, appears, in all conditions.

The plastic deformation of ferrite is mainly controlled by dislocations slip, due to their high stack fault energy (SFE), whereas austenite has different modes of deformation, such as dislocations slip, deformation twins and strain induced martensite transformation [4,8-10]. Other authors report the single-walled Taylor lattice domain boundaries (DB), double-walled microbands (MB) action in synergy with mechanical twins [11].

These austenite strain mechanisms are intrinsically related to its SFE, which depends on the elements present in the austenite at a given temperature [3]. Studies carried out show the predominant mechanism being strain induced martensite for SFE < 20 mJ/m 2 , deformation twinning with SFE between 20-50 mJ/m 2 and dislocations slip for SFE > 50 mJ/m 2 [12].

To calculate the SFE of the steel in this study, the equations proposed by Schramm and Reed [12], Equation 1, and by Rhodes and Thompson [13], Equation 2, were used via EDS chemical analysis (20% Cr, 5% Ni, 2% Mn, 1.5% Mo, 1% Si and balanced Fe) of the austenite phase, obtaining 19 mJ/m 2 and 22 mJ/m 2 , respectively.

Table 1. Chemical composition of 2304 lean duplex stainless steel

Element	C	Cr	Cu	Mo	Si	Ni	Mn	N
wt%	0.011	22.9	0.45	0.28	0.20	4.2	1.5	0.11

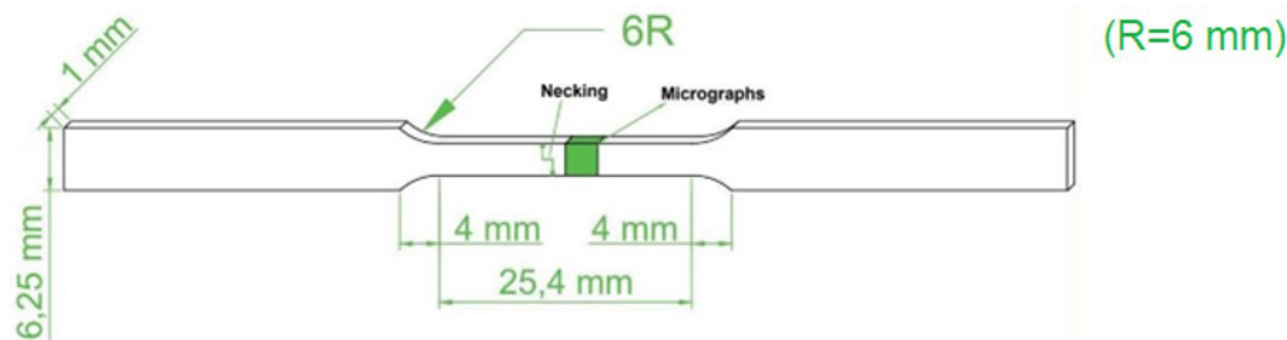


Figure 1. Tensile specimen dimensions and scheme used to withdraw the sections for micrographs of the 2304 LDSS, as-received and cold rolled with different reduction: 4%CR, 12%CR, 17%CR and 22%CR.

$$SFE \left(\frac{mJ}{m^2} \right) = -53 + 6.2(\%Ni) + 0.7(\%Cr) + 3.2(\%Mn) + 9.3(\%Mo) \quad (1)$$

$$SFE \left(\frac{mJ}{m^2} \right) = 1.2 + 1.4(\%Ni) + 0.6(\%Cr) + 17.7(\%Mn) - 44.7(\%Si) \quad (2)$$

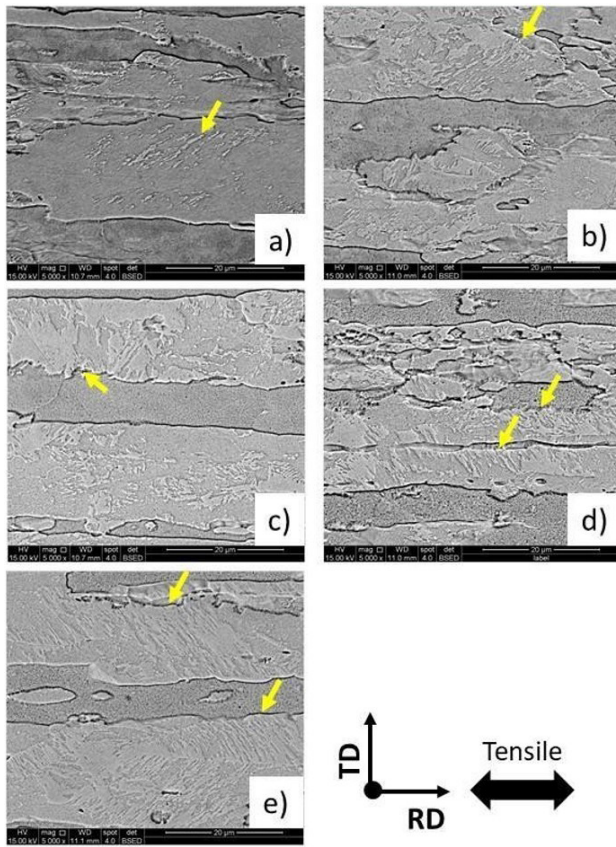


Figure 2. Microstructure of 2304 LDSS cold rolled and tensile tested. (a) AR-T, (b) 4%CR-T, (c) 12%CR-T, (d) 17%CR-T, (e) 22%CR-T.

Observing the SFE values, the studied steel presents the strain induced martensite and deformation twinning as the main mechanisms. This martensitic transformation can occur in two ways: (i) direct transformation to centered-body tetragonal martensite, tcc, $\gamma \rightarrow \alpha'$, by the Kurdjumov-Sachs and Nishiyama-Wassermann orientation relationship $\langle 110 \rangle \gamma // \langle 100 \rangle \alpha'$ [11] and (ii) formation of intermediate martensite, epsilon of hexagonal structure, hc, $\gamma \Rightarrow \epsilon \Rightarrow \alpha'$, which can form due to the metastability of austenite, and following the Shoji-Nishiyama orientation relationship $\langle 110 \rangle \gamma // \langle 2110 \rangle \epsilon$ [5,6,13].

Grain boundaries are known to be a site of α/ϵ -martensite nucleation, since the geometrically necessary dislocations are formed to accommodate strain gradient generated by the deformation of the two phases [10]. Also, on the beginning of deformation, ϵ -martensite embryos generated by the motion of Shockley partial dislocations on two consecutive close packed planes $\{111\} \gamma$ [14,15], are accumulated on the grain boundaries [6]. Thus, making a perfect situation for the α/ϵ -martensite nucleation starts on grain boundaries and grow inside the grain, as it can be seen in the Figure 2, which formed in the boundaries of α/γ and grow into austenitic grain.

Figures 3 and 4 shows EBSD results, containing image quality (IQ), kernel average misorientation (KAM), and phase maps (PM) of the 2304 LDSS samples, as- received and cold rolled, respectively. KAM maps show a microstructural grain refinement, or lamellae thickness reduction, as the cold deformation increase, mainly for 17%CR and 22%CR specimens, Figure 4h and 4k.

Some observations at this point are very important. The first relates to Figure 3 regarding the non-presence of α' -martensite, and much less the α' -martensite. This is because the steel has undergone an industrial homogenization at 1050 °C for 180 s after hot rolling. The microstructure is

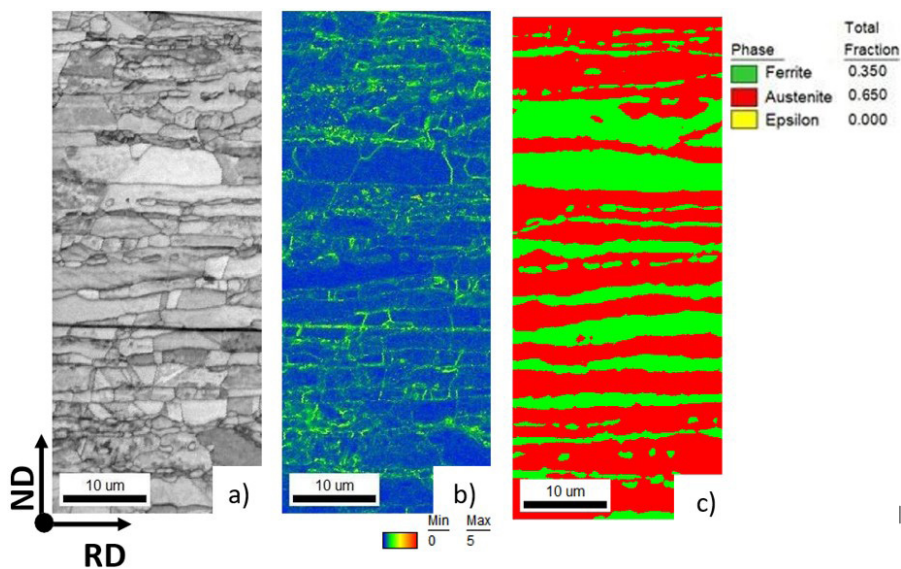


Figure 3. EBSD mapping of 2304 LDSS as-received sample. (a) IQ, (b) kernel average misorientation map, (c) phase map

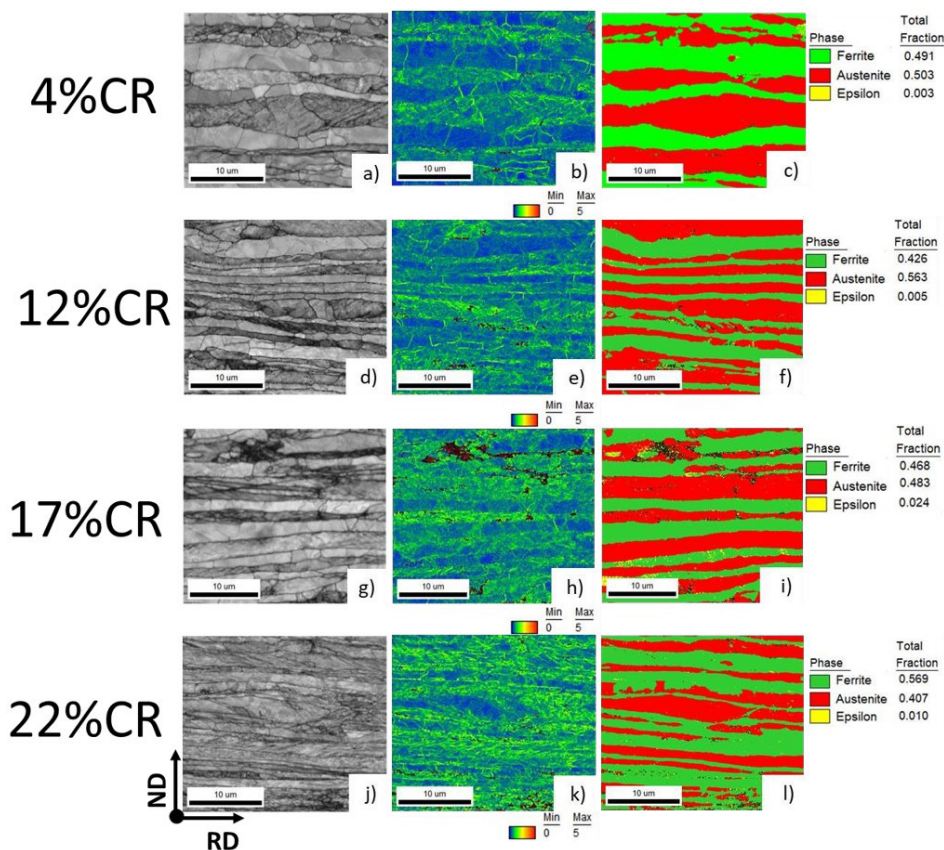


Figure 4. EBSD mapping of 2304 LDSS 4%CR sample. (a,d,g,h) QI, (b,e,h,k) kernel average misorientation map, (c,f,i,l) phase map.

heterogeneous, containing very small and very large grains, Figure 3a. Figure 3b reveals a concentration of crystalline defects in the γ phase and at ferrite-austenite interface. Continuing in the direction of ϵ -martensite formation, it occurs only after cold rolling with 4% reduction (4%CR) (Figure 4b,c), and extend to all other rolling conditions. On sample 17%CR (Figure 4h, i) the ϵ -martensite form with the highest intensity on shear bands, and with a residual fraction in the 22%CR sample (Figure 4k,l). As the deformation increases, austenite grains are filled with shear bands, which resulted in the formation of ϵ - and α' martensite. KAM maps clearly show this occurrence, as the images encompass a smaller fraction of blue areas, or a larger fraction of green areas, including black regions as in Figure 4b,h.

Figure 5 illustrates the KAM graphs distribution, volume fraction versus KAM orientation, of the samples after cold rolling, Figure 5a,c, and cold-rolled plus tensile testing, Figure 5b,d. The local misorientation calculates the average misorientation between each pixel and its neighboring pixels and assigns the average value to that pixel [16]. The ferrite crystals exhibit in-grain orientation gradients which are related to the formation of geometrically necessary dislocations and cell formation. The map of the deformed ferrite (blue areas, Figure 4) shows a substructure consisting of cells or subgrains. Regions with a low QI inside the ferrite grains can be defined as dislocation walls [17,18]. The KAM map of ferrite shows that the highest local

misorientations are located at the γ/γ and γ/α interfaces and at in-grain cell boundaries, where high dislocation densities prevail. The strain at which the α' -martensite starts to form at intersecting ϵ -martensite bands was referred to as transient strain by Stringfellow et al. [19].

The evolution of the KAM distribution is similar for both phases, austenite, and ferrite plus martensite. At low strains the KAM distribution reveals small average values for both phases, less than 1° , Figure 5a,c. This indicates a low dislocation density and a narrow misorientation distribution [20]. The ferrite contains a slightly higher fraction of small in-grain misorientations than the austenite. With increasing strain, after tensile tests, Figure 5b,d, the curves shift towards higher average misorientation angles, reaching 5° , due to an increase in the dislocation density and formation of a new ϵ - and α' -martensite volume fractions. The average misorientation values increase with strain in both phases (Figure 5). At higher strains the austenite reveals slightly higher average KAM values than ferrite. This is mainly attributed to the fact that the austenite accumulates more deformation than the bcc phase, where the martensite is much stronger than austenite and ferrite due to the nature of the transformation, shear, so the strain concentrates in austenite, Figure 5b [15,17,20].

TEM micrographs of the 2304 LDSS cold-rolled samples in different intensity are shown in Figure 6a-l. Analyzing these micrographs, it is possible to observe in sample

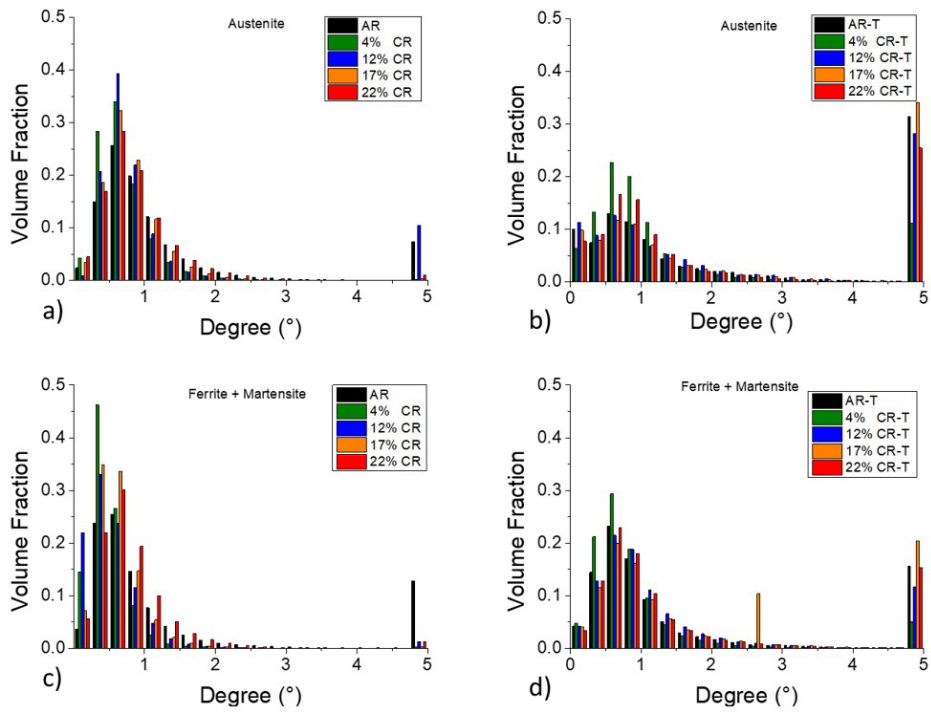


Figure 5. KAM maps of the deformed samples for different reduction levels in (a) and (b) austenite, (c) and (d) ferrite.

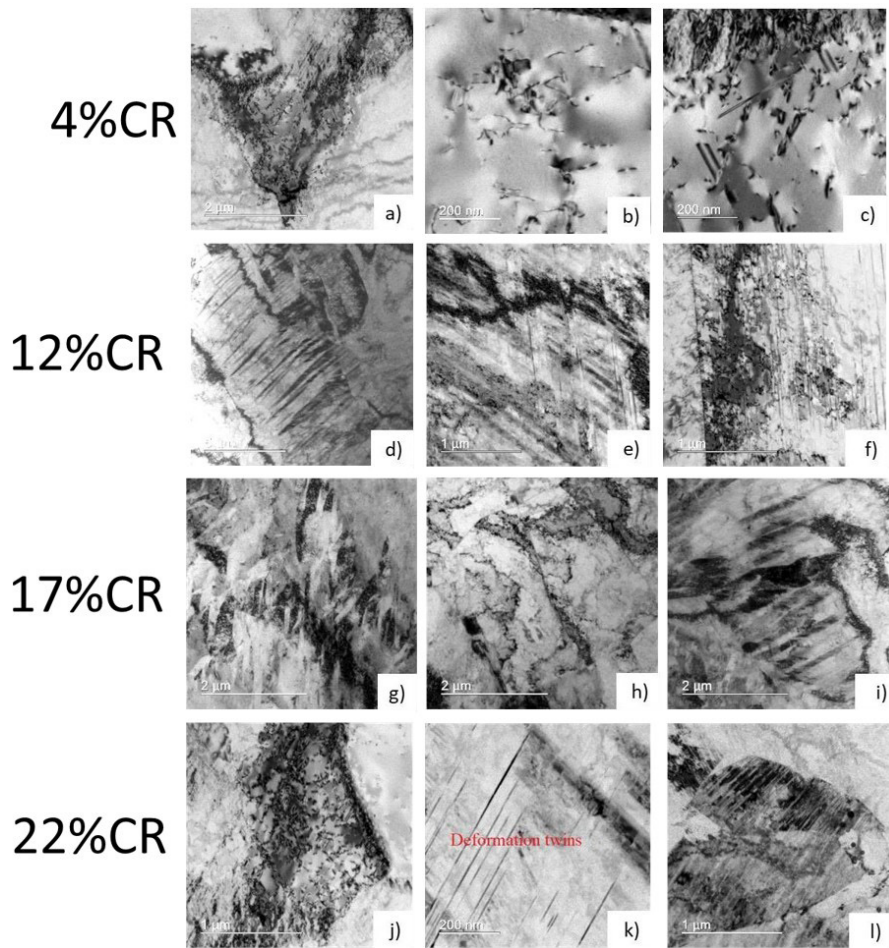


Figure 6. Micrographs obtained via TEM, (a), (b), (c) 4%CR, (d), (e), (f) 12%CR, (g), (h), (i) 17%CR, and (j), (k), (l) 22%CR reduction.

4%CR, already in the first degree of cold deformation, some deformation twins and dense dislocations walls (Figure 6a), discrete dislocations in wavy form with localized areas (Figure 6b) and stacking faults (Figure 6c). In sample with 12%CR strain, α' -martensite was formed at shears bands concentration in form of laths (Figure 6d), and at the intersection of the shear bands, and grain boundaries (Figure 6e-f), a mechanism reported by several authors [4-6,9,14,16,17] for its formation, besides deformation twins (Figure 6f). It is known that deformation twinning, and martensite blocks are barriers to the movement of dislocations, causing them to pile-up at the interface of these microconstituents, leading to an increase in the back-stress, which also contributes to work hardening [3,4].

As the deformation increases, more defects, dislocations, and dislocation tangles, are generated, many dislocations appear inside the grains and at grain boundaries, making it even more difficult to move the dislocations. In the samples with 17%CR and 22%CR deformation, a greater amount of α' -martensite in the form of blocks is observed, Figure 6g-i. In addition to a substructure containing more defects, dislocation tangles (Figure 6j,l). Ferrite phase is dominated by a small amount of entangled and randomly dislocations arrays with wavy configuration like in Figure 6h. Therefore, the strength increases more in austenite phase than in ferrite. This is due to high strain hardening capacity (dislocations generation) of the fcc phase and α' -martensite islands itself formation. Many shear bands occur in the austenite grains with the further increasing of strain (17%CR to 22%CR). While the stacking faults at 4%CR were aligned unidirectionally, those at 22% were developed along two principal directions (Figure 6j,k,l) [11].

Figures 7 and 8 depict the micrographs obtained via TEM of the samples after they were submitted to tensile tests (T), 4%CR-T and 17%CR-T, respectively. Randomly distributed dislocations and some incipient cellular arrangements can be observed in ferrite grains, Figure 7a. By contrast, randomly distributed dislocations forming dense dislocations walls and tangled dislocations arrays appear in ferrite grains, as illustrated in Figure 7b. Some dislocations arrays appear also in austenite (Figure 7h) [11,21]. Shear bands that consist of stacking faults and α' -martensite are clearly visible (Figure 7f,g). In Figure 7f, the martensite appears in form of blocks and lath.

Figure 8 shows typical TEM micrographs of the 2304 LDSS after cold rolling with 17% reduction, plus tensile test specimens. Wide shear bands, Figure 8d,e and annealing twin, Figure 8f, can be observed in austenite grain. By contrast, randomly distributed dislocations forming dense dislocations walls and tangled dislocations arrays appear in ferrite grains, as illustrated in Figure 8a. Some dislocations arrays appear also in austenite (Figure 8h) [11,21] for the specimen 17%CR-T, shown in Figure 8. It is possible to identify a greater number of shear bands and shear band intersections, whose seems to be higher than in the sample deformed with less intensity (4%CR-T). This observation

correlates with the results of Olson and Cohen [14], who observed that the shear band formation is promoted by the high strain. α' -martensite was found to nucleate at the intersections of the shear bands, as shown in Figures 8e and 8d,h, which has been observed also by other researchers [10,11,15], but its nucleation occurs also in shear bands concentration and grain boundaries, as observed before tensile tests.

At a low strain of 4%CR-T, dislocations have equal spacing arrays along two principal directions as seen in Figure 8. This dislocation configuration is typical for planar glide. With increasing strain up to 22%CR, the slip spacing significantly decreased without altering the slip directions. For sure, distinct dislocation cells and mechanical twins were formed. Microstructure at 22%CR strain exhibited well-developed microbands (MB), and their intersections prevailed in tensile sample. MB intersections are known to subdivide the grain and to result in the grain refinement effect [11].

Deformation twins were easily observed in 4%CR-T sample and still to be formed at 22%CR. Above 22%CR strain when the sample was tensile tested, the microstructure was highly populated by well-developed mechanical twins. Generation of the stacking faults at grain boundaries was also observed in the sample deformed to 17%CR-T Figure 8. It indicates that planar glide occurred on a single slip plane at the initial deformation stage and then multiple slip took place on the three principal slip planes of fcc at high strains. These observations evidence planar glide of dislocations on the limited slip systems. After rupture of tensile specimens, the high-density dislocations were distributed throughout matrix, Figures 7 and 8.

Figure 9 shows the X-ray diffraction patterns, Figure 9a for samples before, and Figure 9b, after tensile tests. The peak (111) γ had its intensity decreased due to cold rolling process, and remained extinct after the tensile test, although the peak (220) γ increased on rolling process and became stronger on tensile samples. Regarding to bcc phase, the peak (110) α has also been decreased with rolling reduction, but the major decreasing was on as-received sample (AR) after tensile test. Peaks (200) α and (211) α also increased after tensile test in all samples, which could suggest the strain-induced martensite transformation and texture strengthen of the material [1,8,9].

Table 2 summarizes estimated phase volume fraction obtained by XRD. A slight increase in bcc phases (ferrite and $\alpha\phi$ -martensite) volume fraction was observed with increasing deformation during cold rolling. The main variation of austenite and bcc phases was observed on the AR sample after tensile test, which is another evidence of the TRIP effect [8-10]. Sandim et al. [22] have found a α' -martensite saturation, 25%Vv, on heavy cold-rolled (80%) samples of the same steel, after homogenizing annealing at 1080 °C for 30 s. This amount corresponds to the difference between austenite found on AR and AR-T samples, which is 25%Vv.

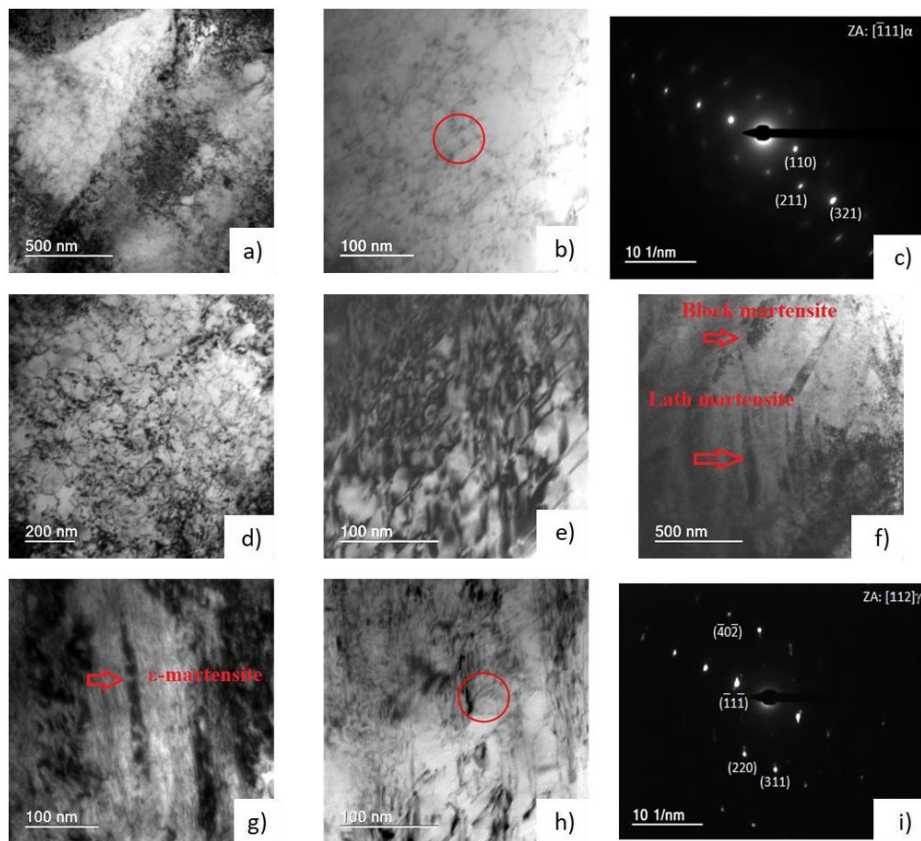


Figure 7. Micrographs obtained via TEM of the sample 4%CR-T.

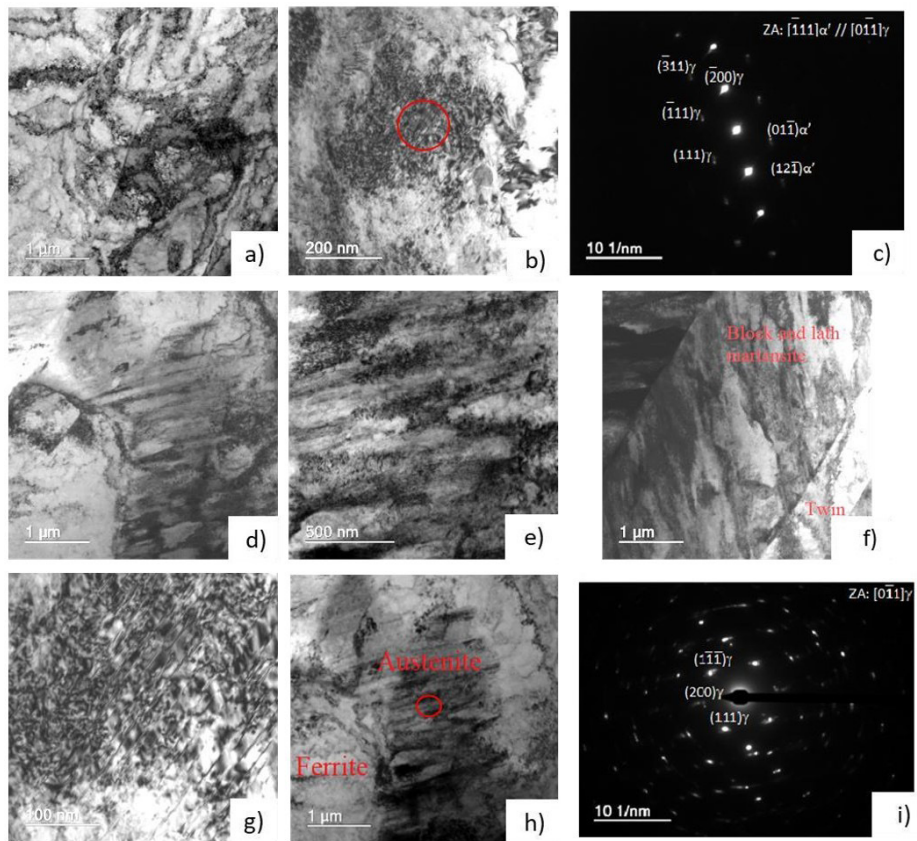


Figure 8. Micrographs obtained via TEM of the sample 17%CR-T.

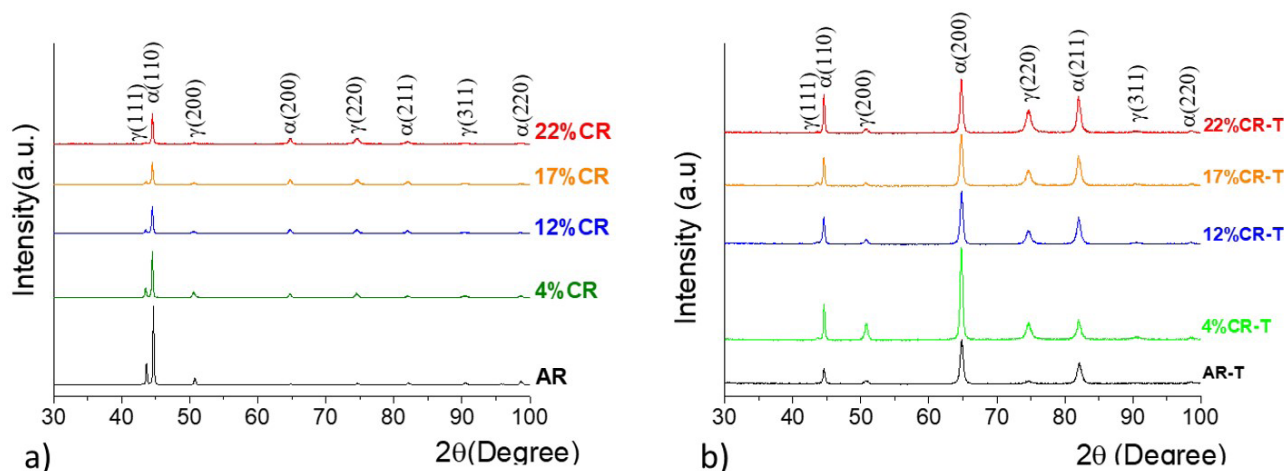


Figure 9. X-ray diffraction patterns of LDSS after different cold rolling reductions, (a) before tensile test, (b) after tensile test.

3.2 Microtexture formation

Maria et al. [5] showed that due to previous deformation by cold rolling process, the texture of γ phase was formed mainly by $\{111\} \langle 112 \rangle$ brass, and S $\{123\} \langle 634 \rangle$, while $\{011\} \langle 100 \rangle$ Goss appeared only on 22% reduction sample [6]. Those textures are typical from deformed fcc materials [23,24]. While α phase had its ND fiber weakened in detriment of strengthening in RD fiber.

Studies showed a highly orientation relationship in transformation of austenite to martensite, both of ϵ , and α'' , which are related by Kurdjumov-Sachs, Nishiyama – Wassermann, and Nishiyama and Pitsch-Schrader [5,6] respectively. So previous texture has major impact on those transformations. Since AR sample had a weak texture due to early homogenization, grains were allowed to fulfil the conditions of the transformation [14,25], as it could be seen on the change of austenite volume fraction in Table 2. Seeing ODFs from Figure 10, after tensile test, AR-T samples have mainly texture around $\{012\} \langle 100 \rangle$, followed by $\{110\} \langle 112 \rangle$ brass. This behavior was seen also in a URN45N duplex stainless steel after tensile test [26]. Even with low cold rolling deformation, austenite acquired strong deformed texture [6], especially the component brass. This orientation was reported to be more stable, and resistant to strain induced martensite transformation [27-29]. On 4%CR-T the only texture present is $\{110\} \langle 112 \rangle$ brass with high intensity (max 25.47), reinforcing this component acquired by cold rolling. On the other hand, 12%CR-T sample shifted from $\{110\} \langle 112 \rangle$ to component $\{110\} \langle 111 \rangle$ A, which appears together with $\{112\} \langle 111 \rangle$ copper [28,30], also $\{110\} \langle 001 \rangle$ Goss was present with lesser intensity. Studies showed that components stability stays in $\langle 100 \rangle$ and $\langle 111 \rangle$ directions during tensile stress [26,31], so the austenite grains were trying to make this change in direction, since in the 17%CR-T sample Goss and $\{110\} \langle 115 \rangle$ G/B were the major components, with a weak component $\{110\} \langle 111 \rangle$ present in ODF. Regarding to 22%CR-T, it was the only

Table 2. Volume fraction of phases after CR and tensile test

Sample / Volume Fraction (%)	Cold-Rolled		Cold-Rolled + Tensile Test	
	γ	$\alpha + \alpha'$	γ	$\alpha + \alpha'$
AR	35	65	10	90
4%CR	33	67	27	73
12%CR	31	69	26	74
17%CR	33	67	26	74
22%CR	27	73	27	73

one which present a strong $\{110\} \langle 001 \rangle$ Goss component already in cold-rolling condition, and after tensile test the $\{100\} \langle 001 \rangle$ cube component was the major one.

Analyzing the texture from bcc phase, some martensite could be detected from ODF by components $\{112\} \langle 110 \rangle$, present on α -fiber, and $\{554\} \langle 225 \rangle$ [28], already detected in AR-T sample, together with $\{001\} \langle 110 \rangle$ rotated cube.

3.3 Mechanical properties evaluation

Microhardness of all samples are shown on Figure 11, and it could be seen a progressive strengthening of hardness on each sample after cold rolling, where the main gain is observed from the 12%CR reduction sample. Maria et al. [5] have found in 12%CR sample blocks of α' -martensite, which could explain this notorious increase in hardness [13,14,22]. Although, 4%CR sample has some martensite found in other study [6], its mainly crystalline defects, as could be seen in Figure 6b,c, are dislocations piled-up and stacking faults, and some deformation twins.

Figure 12 depicts the true stress-strain curves, showing the reduction in ductility and the increase in strength for the most deformed sample. The summary of their properties is listed in Table 3, which showed a significant increase in the yield strength and decrease in the total elongation as the cold rolling reduction increases, mainly due to strain hardening and strain induced martensite transformation (SIMT) in the

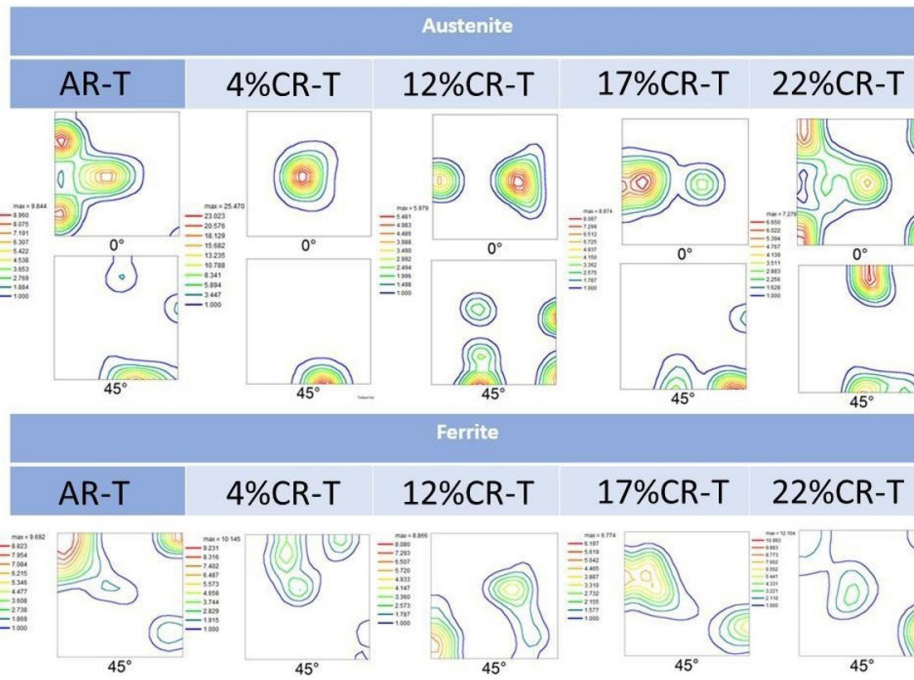


Figure 10. Microtexture expressed as ODF from samples after tensile test.

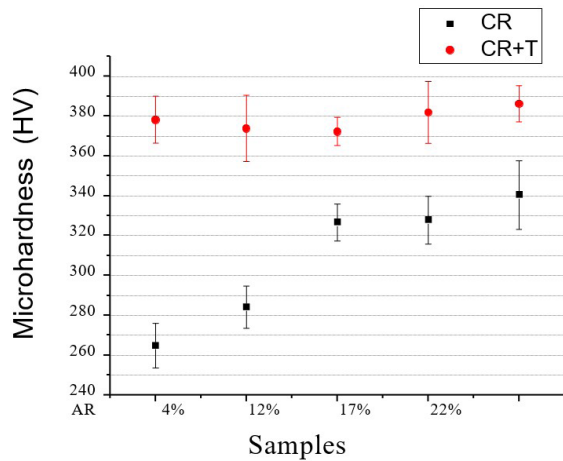


Figure 11. Microhardness of sample cold-rolled, and cold-rolled plus tensile test.

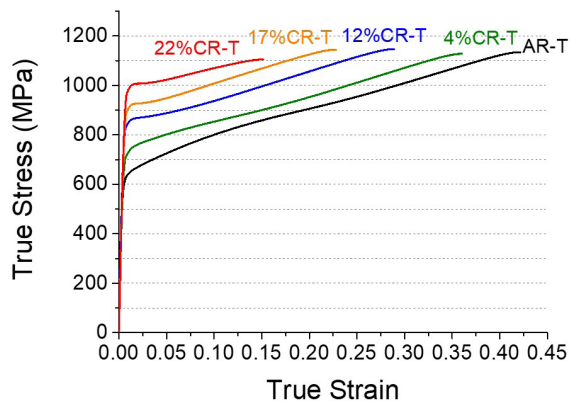


Figure 12. Flow curves of the 2304 lean DSS for different reductions applied by cold rolling.

Table 3. Summary of mechanical properties obtained after the tensile test

Sample	YS (MPa)	UTS (MPa)	UE (%)	TE (%)	YS/UTS
AR	600 ± 4	753 ± 7	45 ± 1	57 ± 1	0,80
4%	706 ± 6	796 ± 6	37 ± 2	38 ± 1	0,87
12%	820 ± 3	867 ± 2	25 ± 1	29 ± 1	0,95
17%	878 ± 6	922 ± 3	19 ± 1	20 ± 1	0,95
22%	929 ± 18	960 ± 19	9 ± 1	16 ± 1	0,97

austenite phase. After 4%CR deformation, YS increased by 18% and the total elongation was reduced by 33%. After 22%CR deformation, YS increased by 55% and the total elongation was reduced by almost 73%. Note the increase in the YS/UTS with the increase of deformation, which reflects in the decrease of the steel work hardening capacity [19]. However, there is also a smooth transition between the elastic and plastic regime for the AR-T and 4%CR-T samples, unlike the 12%CR-T, 17%CR-T and 22%CR-T deformed samples, where a stress peak is observed.

When plotting the flow curves, Figure 12, the sigmoidal shape is evident for all samples. In the strain hardening curves (Figure 13) the inflexion points, where the curve changes its behavior from a parabolic to sigmoidal shape, marks this transient strain regime [20]. Such behavior suggests the presence of the TWIP/TRIP effect [8,10,17].

In addition to this sigmoidal shape, the samples with 12%CR-T, 17%CR-T and 22%CR-T deformation showed a plateau at the beginning of plastic deformation.

To analyze the strain hardening, the flow curves were derived, which presented two distinct behaviors. The AR-T and 4%CR-T samples had similar behavior and

were divided into four stages, as shown in Figure 13a. Stage I was characterized as a vertical drop in the strain hardening rate (θ) right at the beginning of the deformation. In this stage, of low deformation, the strain is mainly concentrated in austenite [1,5] and the rapid decrease in θ is caused by formation of Shockley partials, and dislocation slipping which interacted causing dynamic strain softening [32-35].

In stage II, the 4%CR-T sample presented a concave shape until reaching a minimum value with $\varepsilon = 0.12$, a smaller extension than AR-T sample, which presented a linear behavior, and reached this minimum at $\varepsilon = 0.18$. This reduction in stage II for 4%CR-T sample may be related to the presence of deformation bands, which in part precedes the formation of ε -martensite. They are sites for nucleation of α' -martensite [6], but the quantification of this occurrence is hard to measure as a function of its very small volume fraction. For all stage of strain hardening the dislocation glide is always present, as the TEM micrographs revealed, Figures 6-8. Since in a previous study, parallel shear bands formation was found to occur after a certain critical stress level was reached, which is in accordance with α' -martensite formation starting in stage II. Therefore, the formation of α' -martensite certainly contributes to strain hardening in stage II, in conjunction with dislocation glide [34]. Stage III, which obtained the same extension for both samples, was defined by increasing the work-hardening rate to a maximum. This stage was related to the formation of α' -martensite [27,36]. Stage IV, which has a sharp drop of θ and a very similar extension for the two samples, this occurs early on the sample with 4%CR-T reduction, since previous defects were introduced in the microstructure and anticipating the formation of α' -martensite, seeing on the reduction of stage II. Choi et al. [10] observed this same decay in θ , and related it to the saturation of martensite promoted by the TRIP effect, leading to the hardening of the remaining austenite and ferrite as the main deformation mechanism at this stage, which has a lower strain hardening rate than the TRIP effect. The summary of the intervals of

these stages is presented in Table 4. The interaction of the martensite and ferrite generates an earlier necking, which will be discussed on the following sections, and corroborates with the decreases of total elongation compared with AR-T sample as could be seen in Table 3. In addition to the end strain induced martensite transformation [4,18,19,22,32-35,37].

The interaction between austenite and ferrite becomes considerably evident when the strain further increases after both constituent phases yielding because of the back stress and forward stress in austenite and ferrite, respectively, which are generated by the pile-up of the geometrically necessary dislocations. The strain initiated in the austenite grains spreads into the adjacent ferrite grains leading to α starts to yield [38].

Samples 12%CR-T, 17%CR-T and 22%CR-T were divided in three stages, Figure 13b. Stage A presented a strong fall at the beginning of deformation, greater than samples AR-T and 4%CR-T. This behavior may be related to abrupt transition between the elastic and plastic regime, which is observed in the flow curves (Figure 12). Stage B, on the other hand, is characterized by an increase of θ , up to a maximum. Järvenpää et al. [27] found similar behavior on austenitic stainless steel 301LN with small cold-rolled reductions (32, 45 and 63%), annealed at 750 °C for 0.1 s, which did not achieved fully recrystallization. The authors found that a higher transformation rates of α' -martensite related with this behavior, which are in accordance with the previous defects generated by cold rolling (Figure 6).

Table 4. True strain values for each stage for the AR-T and 4%CR-T samples

Stage	AR-T	4%CR-T	Range	
			AR 4%	
I	$0,002 < \varepsilon < 0,0150$	$0,002 < \varepsilon < 0,016$	0,015	0,016
II	$0,015 < \varepsilon < 0,184$	$0,016 < \varepsilon < 0,118$	0,169	0,102
III	$0,184 < \varepsilon < 0,341$	$0,118 < \varepsilon < 0,268$	0,157	0,150
IV	$0,341 < \varepsilon < 0,419$	$0,268 < \varepsilon < 0,359$	0,078	0,091

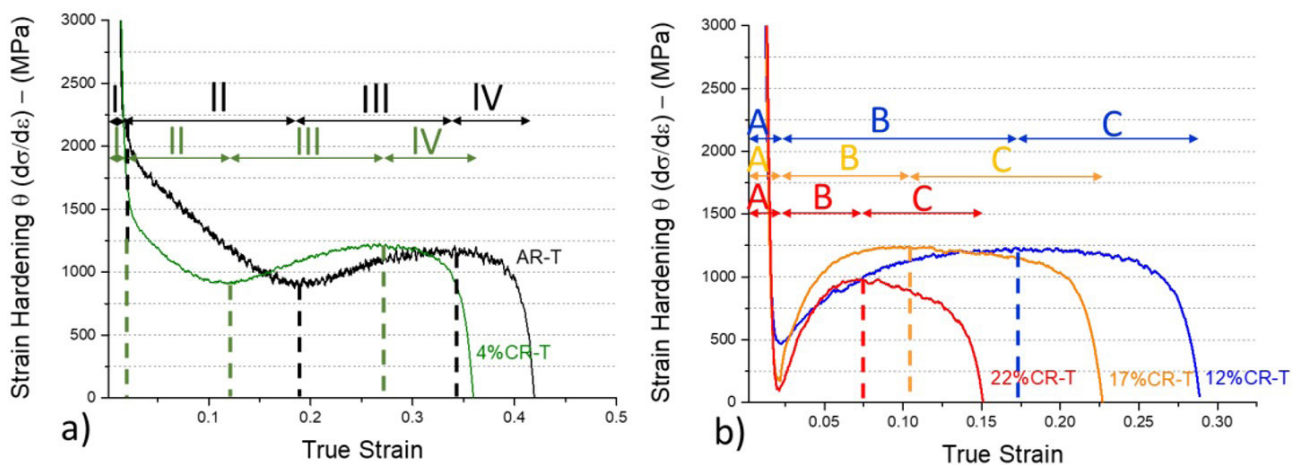


Figure 13. Work hardening rate as a function of true deformation of (a) AR-T and 4%CR-T ; (b) 12%CR-T, 17%CR-T, and 22%CR-T reduction samples.

Challa et al. [39] observed a similar behavior in austenitic stainless steels with a nanograins microstructure, and ultrafine grains with an average grain size of 320 nm, associating the deformation mechanism mainly to the deformation twins.

Furthermore, the new martensite formed by strain in the tensile test tend to be harder than those formed previously, considering that it inherits the structure of dislocations of the austenite that formed it [19]. The extension of stage B is inversely proportional to the deformation of the samples and may be associated with the previous deformation by cold rolling which generated a deformed texture [6,40], especially brass and Goss [27,41], which difficult the transformation of austenite to martensite. Also considering that their microstructures was already more deformed and with the presence of martensite and deformation twins, which hinder the movement of dislocations. Stage C was defined from the drop in the work hardening rate, and have similar explanation as for the stage IV, discussed before, in AR-T and 4%CR-T samples. The summary of each stage is pointing out in Table 5. Also, a scheme of microstructure evolution is shown on Figure 14.

As could be seen for its SFE values, in addition to Figure 13, the steel has different mechanism of deformation, which is difficult to interpret using modelling like Hollomon, Crussard-Jaoult (C-J) analysis, and modified C-J analysis due to the variation of the strain-hardening exponent along the deformation. Stachowicz [41] used a differential n value independent of strain hardening laws, as (Equation 3):

$$n(\varepsilon) = \frac{d \ln \sigma}{d \ln \varepsilon} \quad (3)$$

Where σ and ε are the true stress and strain, respectively, $d\sigma/d\varepsilon$ is the strain hardening rate, and $n(\varepsilon)$ is the instantaneous strain hardening exponent, considering the strain rate and temperature constant.

Plotting the instantaneous strain hardening exponent in Figure 15, it is noticing the different stages during the tensile test, and they are close related with strain hardening rate. The initial drop on $n(\varepsilon)$, belongs to the same range of stage I and stage A of strain hardening rate (Figure 13). As discussed early, this phenomenon is related to dynamic strain softening, such as dislocations annihilation [4,32-35], and by formation of Shockley partials dislocations, which are energetically favored as they are $afcc/6 \langle 112 \rangle$, and requires less energy to be formed [33,35,41-44], and were already formed by cold-rolling in the other samples. The first increase of $n(\varepsilon)$ on AR-T and 4%CR-T has the same range for stage II and some authors related it to the formation of

ε -martensite [10] and is more pronounced on AR-T which had less defects, like shear bands, and α' -martensite formed by cold rolling (Figure 6a,b,c), presented in sample 4%CR, for instance. This behavior postpones the necking and gives an increase on ductility.

The formation of α' -martensite is related to the second increase of $n(\varepsilon)$, after the inflection on AR-T sample ($\varepsilon = 0,18$), and a slight increment on sloop after $\varepsilon = 0,12$. The instantaneous strain hardening exponent is higher in 4%CR-T sample, in comparison with the AR-T, probably due to the deformation of α' -martensite previously formed. The final decrease of $n(\varepsilon)$ starts in the same deformation as stage IV and happens on necking beginning. Regarding to samples 12%CR-T, 17%CR-T, and 22%CR-T the instantaneous hardening exponent is also related to Θ stages, but it values are lower than those achieved by AR-T and 4%CR-T samples, being smaller with the increase of cold-rolling deformation due to the difficult of SIM formation, as well as the previous deformation that already generated some blocks of α' -martensite.

3.4 Fractography analysis

In Figure 16 it is possible to observe the fractography of the samples that present a quasi- cleavage behavior, where the microstructure becomes more brittle as the cold deformation of the samples increases. Strain induced martensite has a greater strength and reduces the crack propagation. In addition, several microvoids emerged, which are represented in Figure 16 by dark spots or regions. Research works related to the morphology of martensite with the fracture surface found that block martensite tends to generate more microcavities [45,46].

Phase boundary and grain boundary sliding is the dominant fracture mechanism. The strain-induced martensite improves the strength by either hindering the crack propagation or reducing the crack growth rate and its path. The fractography of matching fracture surfaces shows a mixture of dimple fracture in ferrite and austenite phases. The crack path of tested specimens resulted in a typical brittle quasi- cleavage fracture surface in the ferritic phase, following by induction of microcracks in the austenite grain crossing the ferritic-austenitic boundary. Finally, the crack propagates through the austenite grain [17,18,38,41,45,46].

Table 5. True strain values for each stage for the 12%CR-T, 17%CR-T and 22%CR-T samples

Stage	12%CR-T	17%CR-T	22%CR-T	Range		
				12%CR-T	17%CR-T	22%CR-T
A	0,002 < ε < 0,022	0,002 < ε < 0,022	0,002 < ε < 0,021	0,022	0,022	0,021
B	0,022 < ε < 0,177	0,022 < ε < 0,103	0,020 < ε < 0,070	0,155	0,081	0,050
C	0,177 < ε < 0,289	0,103 < ε < 0,227	0,070 < ε < 0,150	0,112	0,124	0,08

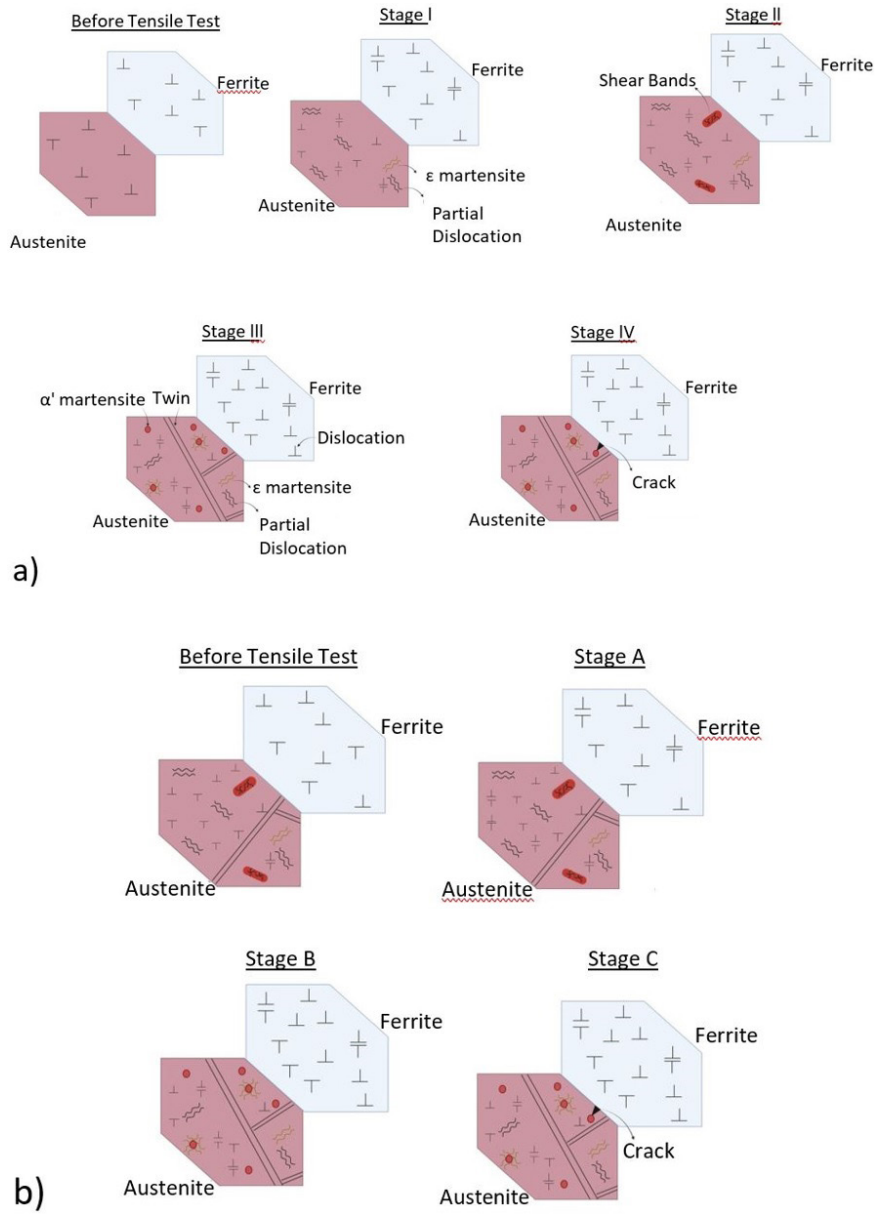


Figure 14- Scheme of the microstructure evolution (a) CF-T, 4%; (b) 12%-T, 17%-T, 22%-T.

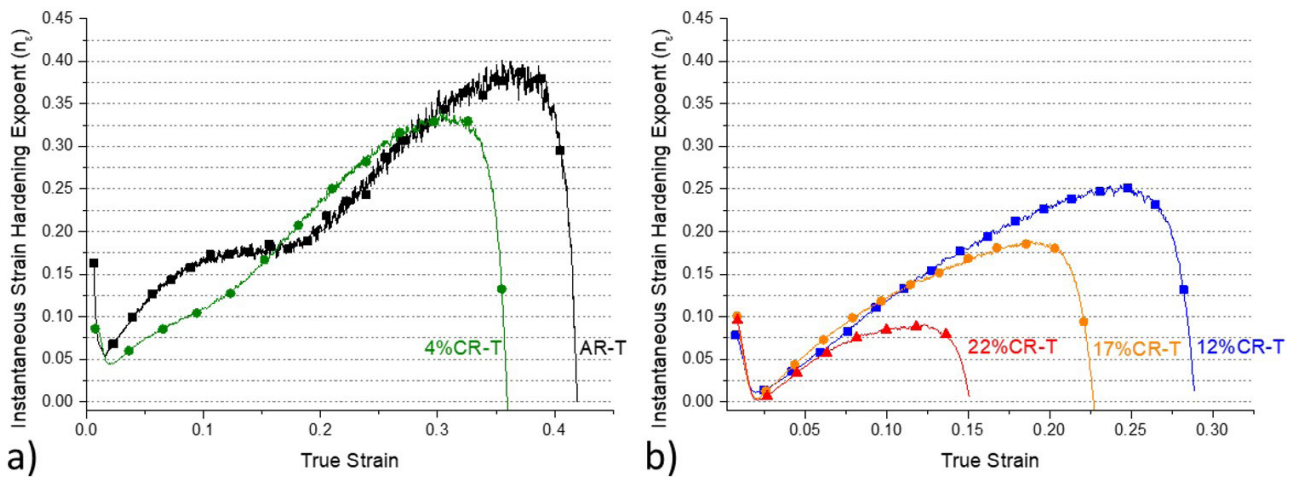


Figure 15. Instantaneous strain hardening exponent (a) AR-T and 4%CR-T, (b) 12%CR-T, 17%CR-T, and 22%CR-T reduction.

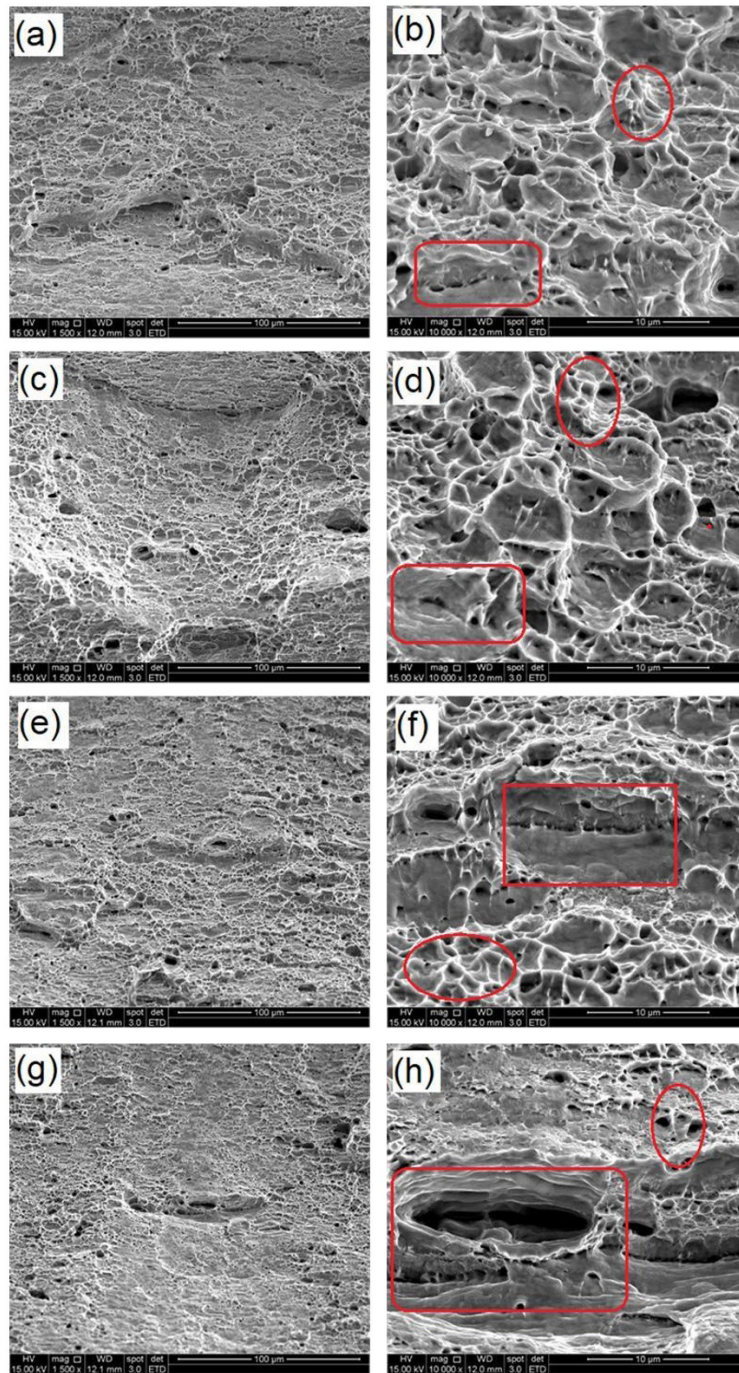


Figure 16. Fractography after tensile testing of the samples with (a,b) 4%CR-T, (c,d) 12%CR-T, (e,f) 17%CR-T and (g,h) 22%CR-T reduction by cold rolling.

4 Conclusions

- At low levels of cold rolling, it was possible to observe the presence of both the TWIP and TRIP effects during tensile tests due to the EFE values.
- It was observed, via X-ray diffraction, a slight increase in the volume fraction of ferrite along the deformation process, but no ϵ -martensite was detected with this

technique. Deformation twins were observed at low deformation levels in 4% cold-rolled sample, which possibly caused the anticipation of the TRIP effect in the steel.

- Small amounts of α' and ϵ was found on 4% reduction by cold rolling, but did not impact on strain hardening behavior, since major defects were stacking faults, deformation twins, and dislocations, which possibly caused the anticipation of the TRIP effect in the steel.

- Previous deformed texture, mainly $\{011\}\langle 211\rangle$ brass, compromised strain induced martensite transformation by tensile test.
- Two different strain hardening behavior were noticed during the tensile tests for the analyzed samples. For samples as-received and 4% cold rolled, 4 stages were obtained, and for samples with 12%, 17% and 22% of cold rolling, 3 stages along the strain hardening were identified.
- α' -martensite blocks, generated by cold rolling with 12%, 17% and 22% thickness reduction, which prevent the movement of dislocations and inhibit the TRIP effect for these samples, directly affected the strain hardening behavior of these samples.
- All samples showed fracture regions with dimples, areas of quasi-cleavage and facets of cleavage, and

the presence of microvoids, due to the α' -martensite in form of blocks present in the microstructure.

Aknowledgements

The authors thank FAPEMIG, CNPq and CAPES for their research support; Microscopy Center of UFMG for TEM examination, and Aperam South America SA for providing lean duplex stainless steel samples.

Data Availability

The raw/processed data required to reproduce these findings cannot be shared at this time due to technical or time limitations.

References

- 1 Zhao Y, Zhang W, Liu X, Liu Z, Wang G. Development of TRIP-aided lean duplex stainless steel by twin-roll strip casting and its deformation mechanism. *Metallurgical and Materials Transactions. A, Physical Metallurgy and Materials Science*. 2016;47:6292-6303. <http://dx.doi.org/10.1007/s11661-016-3771-5>.
- 2 Liljas M, Johansson P, Liu H-P, Olsson C-OA. Development of a lean duplex stainless steel. *Steel Research International*. 2008;79:466-473. <http://dx.doi.org/10.1002/srin.200806154>.
- 3 Charles J. Duplex stainless steels, a review after DSS'07 held in Grado. *Revue de metallurgie*. 2008;105:155-171. <http://dx.doi.org/10.1051/metal:2008028>.
- 4 Pierce DT, Jiménez JA, Bentley J, Raabe D, Wittig JE. The influence of stacking fault energy on the microstructural and strain-hardening evolution of Fe-Mn-Al-Si steels during tensile deformation. *Acta Materialia*. 2015;100:178-190. <http://dx.doi.org/10.1016/j.actamat.2015.08.030>.
- 5 Maria GGB, Rodrigues DG, Freitas ÉTF, Santos DB. ϵ -Martensite formation for low strains in a lean duplex stainless steel. *Materials Letters*. 2019;234:283-286. <http://dx.doi.org/10.1016/j.matlet.2018.09.104>.
- 6 Rodrigues DG, Maria GGB, Viana NAL, Santos DB. Effect of low cold-rolling strain on microstructure, texture, phase transformation, and mechanical properties of 2304 lean duplex stainless steel. *Materials Characterization*. 2019;150:138-149. <http://dx.doi.org/10.1016/j.matchar.2019.02.011>.
- 7 American Society for Testing and Materials. ASTM E8/E8M standard test methods for tension testing of metallic materials. West Conshohocken: ASTM; 2010. <https://doi.org/10.1520/E0008>
- 8 Lechartier A, Meyer N, Estevez R, Mantel M, Martin G, Parry G, et al. Deformation behavior of lean duplex stainless steels with strain induced martensitic transformation: role of deformation mechanisms, alloy chemistry and predeformation. *Materialia*. 2019;5:100190. <http://dx.doi.org/10.1016/j.mtla.2018.100190>.
- 9 Maria GGB, Pedroso CAD, Rodrigues DG, Santos DB. Strain-induced martensite and reverse transformation in 2304 lean duplex stainless steel and its influence on mechanical behavior. *Steel Research International*. 2019;90:1-11. <http://dx.doi.org/10.1002/srin.201800437>.
- 10 Choi JY, Ji JH, Hwang SW, Park KT. TRIP aided deformation of a near-Ni-free, Mn-N bearing duplex stainless steel. *Materials Science and Engineering A*. 2012;535:32-39. <http://dx.doi.org/10.1016/j.msea.2011.12.037>.
- 11 Park KT, Jin KG, Han SH, Hwang SW, Choi K, Lee CS. Stacking fault energy and plastic deformation of fully austenitic high manganese steels: effect of Al addition. *Materials Science and Engineering A*. 2010;527:3651-3661. <http://dx.doi.org/10.1016/j.msea.2010.02.058>.
- 12 Schramm RE, Reed RP. Stacking fault energies of seven commercial austenitic stainless steels. *Metallurgical Transactions. A, Physical Metallurgy and Materials Science*. 1975;6:1345-1351. <http://dx.doi.org/10.1007/BF02641927>.

- 13 Rhodes CG, Thompson AW. The composition dependence of stacking fault energy in austenitic stainless steels. *Metallurgical Transactions. A, Physical Metallurgy and Materials Science*. 1977;8:1901-1906. <http://dx.doi.org/10.1007/bf02646563>.
- 14 Olson GB, Cohen M. A general mechanism of martensitic nucleation: Part I. General concepts and the FCC \rightarrow HCP transformation. *Metallurgical Transactions. A, Physical Metallurgy and Materials Science*. 1976;7:1897-1904. <http://dx.doi.org/10.1007/BF02659822>.
- 15 Talonen J, Hänninen H. Formation of shear bands and strain-induced martensite during plastic deformation of metastable austenitic stainless steels. *Acta Materialia*. 2007;55:6108-6118. <http://dx.doi.org/10.1016/j.actamat.2007.07.015>.
- 16 Wright SI, Nowell MM, Field DP. A review of strain analysis using electron backscatter diffraction. *Microscopy and Microanalysis*. 2011;17:316-329. <http://dx.doi.org/10.1017/S1431927611000055>.
- 17 Gao Z, Li J, Chen Y, Wang Y. Effect of dual-phase structure on the microstructure and deformation inhomogeneity of 2507 duplex stainless steel. *Ironmaking & Steelmaking*. 2021;48:393-401. <http://dx.doi.org/10.1080/03019233.2020.1794766>.
- 18 Jia Q, Wang Y, Mei R, Chen L, Hao S, Zhang H, et al. The dependences of deformation temperature on the strain-hardening characteristics and fracture behavior of Mn–N bearing lean duplex stainless steel. *Materials Science and Engineering A*. 2021;819:141440. <http://dx.doi.org/10.1016/j.msea.2021.141440>.
- 19 Stringfellow RG, Parks DM, Olson GB. A constitutive model for transformation plasticity accompanying strain-induced martensitic transformations in metastable austenitic steels. *Acta Metallurgica et Materialia*. 1992;40:1703-1716. [http://dx.doi.org/10.1016/0956-7151\(92\)90114-T](http://dx.doi.org/10.1016/0956-7151(92)90114-T).
- 20 Herrera C, Ponge D, Raabe D. Design of a novel Mn-based 1 GPa duplex stainless TRIP steel with 60% ductility by a reduction of austenite stability. *Acta Materialia*. 2011;59:4653-4664. <http://dx.doi.org/10.1016/j.actamat.2011.04.011>.
- 21 Choi JY, Ji JH, Hwang SW, Park KT. Strain induced martensitic transformation of Fe-20Cr-5Mn-0.2Ni duplex stainless steel during cold rolling: Effects of nitrogen addition. *Materials Science and Engineering A*. 2011;528:6012-6019. <http://dx.doi.org/10.1016/j.msea.2011.04.038>.
- 22 Sandim MJR, Souza Filho IR, Mota CFGS, Zilnyk KD, Sandim HRZ. Microstructural and magnetic characterization of a lean duplex steel: strain- induced martensite formation and austenite reversion. *Journal of Magnetism and Magnetic Materials*. 2021;517. <http://dx.doi.org/10.1016/j.jmmm.2020.167370>.
- 23 Fargas G, Akdut N, Anglada M, Mateo A. Microstructural evolution during industrial rolling of a duplex stainless steel. *ISIJ International*. 2008;48:1596-1602. <http://dx.doi.org/10.2355/isijinternational.48.1596>.
- 24 Hirsch J, Lücke K. Mechanism of deformation and development of rolling textures in polycrystalline f.c.c. metals-I. Description of rolling texture development in homogeneous CuZn alloys. *Acta Metallurgica*. 1988;36:2863-2882. [http://dx.doi.org/10.1016/0001-6160\(88\)90172-1](http://dx.doi.org/10.1016/0001-6160(88)90172-1).
- 25 Olson GB, Cohen M. A general mechanism of martensitic nucleation: Part II. FCC \rightarrow BCC and other martensitic transformations. *Metallurgical Transactions. A, Physical Metallurgy and Materials Science*. 1976;7:1905-1914. <http://dx.doi.org/10.1007/BF02654988>.
- 26 Wroński S, Tarasiuk J, Bacroix B, Baczmański A, Braham C. Investigation of plastic deformation heterogeneities in duplex steel by EBSD. *Materials Characterization*. 2012;73:52-60. <http://dx.doi.org/10.1016/j.matchar.2012.07.016>.
- 27 Järvenpää A, Jaskari M, Karjalainen LP. Reversed microstructures and tensile properties after various cold rolling reductions in AISI 301LN steel. *Metals*. 2018;8. <http://dx.doi.org/10.3390/met8020109>.
- 28 Järvenpää A, Jaskari M, Man J, Karjalainen LP. Austenite stability in reversion-treated structures of a 301LN steel under tensile loading. *Materials Characterization*. 2017;127:12-26. <http://dx.doi.org/10.1016/j.matchar.2017.01.040>.
- 29 Poulon-Quintin A, Brochet S, Vogt JB, Glez JC, Mithieux JD. Fine grained austenitic stainless steels: the role of strain induced α' martensite and the reversion mechanism limitations. *ISIJ International*. 2009;49:293-301. <http://dx.doi.org/10.2355/isijinternational.49.293>.
- 30 Somani MC, Juntunen P, Karjalainen LP, Misra RDK, Kyröläinen A. Enhanced mechanical properties through reversion in metastable austenitic stainless steels. *Metallurgical and Materials Transactions. A, Physical Metallurgy and Materials Science*. 2009;40:729-744. <http://dx.doi.org/10.1007/s11661-008-9723-y>.
- 31 Poudens A, Bacroix B, Bretheau T. Influence of microstructures and particle concentrations on the development of extrusion textures in metal matrix composites. *Materials Science and Engineering A*. 1995;196:219-228. [http://dx.doi.org/10.1016/0921-5093\(94\)09703-8](http://dx.doi.org/10.1016/0921-5093(94)09703-8).

- 32 Zhang W, Hu J. Effect of annealing temperature on transformation induced plasticity effect of a lean duplex stainless steel. *Materials Characterization*. 2013;79:37-42. <https://doi.org/10.1016/j.matchar.2013.02.003>.
- 33 De AK, Speer JG, Matlock DK, Murdock DC, Mataya MC, Comstock RJ. Deformation-induced phase transformation and strain hardening in type 304 austenitic stainless steel. *Metallurgical and Materials Transactions. A, Physical Metallurgy and Materials Science*. 2006;37:1875-1886. <http://dx.doi.org/10.1007/s11661-006-0130-y>.
- 34 Soares GC, Rodrigues MCM, Santos LA. Influence of temperature on mechanical properties, fracture morphology and strain hardening behavior of a 304 stainless steel. *Materials Research*. 2017;20:141-151. <http://dx.doi.org/10.1590/1980-5373-mr-2016-0932>.
- 35 Kocks UF, Mecking H. Physics and phenomenology of strain hardening: the FCC case. *Progress in Materials Science*. 2003;48:171-273. [http://dx.doi.org/10.1016/S0079-6425\(02\)00003-8](http://dx.doi.org/10.1016/S0079-6425(02)00003-8).
- 36 Martin S, Wolf S, Martin U, Krüger L, Rafaja D. Deformation mechanisms in austenitic TRIP/TWIP steel as a function of temperature. *Metallurgical and Materials Transactions. A, Physical Metallurgy and Materials Science*. 2016;47:49-58. <http://dx.doi.org/10.1007/s11661-014-2684-4>.
- 37 Gutierrez-Urrutia I, Raabe D. Multistage strain hardening through dislocation substructure and twinning in a high strength and ductile weight-reduced Fe-Mn- Al-C steel. *Acta Materialia*. 2012;60:5791-5802. <http://dx.doi.org/10.1016/j.actamat.2012.07.018>.
- 38 Eskandari Sabzi H, Zarei-Hanzaki A, Kajjalainen A, Kisko A. The valuation of microstructural evolution in a thermo-mechanically processed transformation- twinning induced plasticity steel during strain hardening. *Materials Science and Engineering A*. 2019;754:799-810. <http://dx.doi.org/10.1016/j.msea.2018.09.068>.
- 39 Challa VSA, Wan XL, Somani MC, Karjalainen LP, Misra RDK. Strain hardening behavior of phase reversion-induced nanograined/ultrafine-grained (NG/UFG) austenitic stainless steel and relationship with grain size and deformation mechanism. *Materials Science and Engineering A*. 2014;613:60-70. <http://dx.doi.org/10.1016/j.msea.2014.06.065>.
- 40 Rodrigues DG, Maria GGB, Viana NAL, Santos DB. Effect of low cold- rolling strain on microstructure, texture, phase transformation, and mechanical properties of 2304 lean duplex stainless steel. *Materials Characterization*. 2019;150:138-149. <http://dx.doi.org/10.1016/j.matchar.2019.02.011>.
- 41 Stachowicz F. Instantaneous plastic flow properties of thin brass sheets under uniaxial and biaxial testing. *Acta Mech. Slovaca*. 2011;15:22-27. <http://dx.doi.org/10.21496/ams.2011.003>.
- 42 Pérez Escobar D, Silva Ferreira De Dafé S, Verbeken K, Brandão Santos D. Effect of the cold rolling reduction on the microstructural characteristics and mechanical behavior of a 0.06%C-17%Mn TRIP/TWIP steel. *Steel Research International*. 2016;87:95-106. <http://dx.doi.org/10.1002/srin.201400555>.
- 43 Zhang X, Wang P, Li D, Li Y. Multi-scale study on the heterogeneous deformation behavior in duplex stainless steel. *Journal of Materials Science and Technology*. 2021;72:180-188. <http://dx.doi.org/10.1016/j.jmst.2020.09.023>.
- 44 Olson GB, Cohen M. A general mechanism of martensitic nucleation: Part III. Kinetics of martensitic nucleation. *Metallurgical Transactions. A, Physical Metallurgy and Materials Science*. 1976;7:1915-1923. <http://dx.doi.org/10.1007/BF02659824>.
- 45 Liu H, Liu B, Bai P, Sun H, Li D, Sun F, et al. Martensitic transformation and fractographic analysis of lean duplex stainless steel during low temperature tension deformation. *Materials Characterization*. 2015;107:262-269. <http://dx.doi.org/10.1016/j.matchar.2015.07.019>.
- 46 Ding H, Ding H, Song D, Tang Z, Yang P. Strain hardening behavior of a TRIP/TWIP steel with 18.8% Mn. *Materials Science and Engineering A*. 2011;528:868-873. <http://dx.doi.org/10.1016/j.msea.2010.10.040>.

Received: 27 Jun. 2022

Accepted: 31 Ago. 2022